TURBOMACHINERY & PUMP SYMPOSIA | HOUSTON, TX
SEPTEMBER 13-15, 2022
SHORT COURSES: SEPTEMBER 12, 2022

PREDICTION OF LATERAL VIBRATION BEHAVIOR OF INTEGRALLY GEARED CENTRIFUGAL COMPRESSOR DURING SYNCHRONOUS MOTOR STARTUP BY TRANSIENT TORSIONAL-LATERAL COUPLED ANALYSIS

Akira Adachi
Associate Principal Engineer
Toyo Engineering Corporation
Narashino, Chiba, Japan

Yoshitaka Baba
Senior Manager
Kobe Steel, Ltd.
Takasago, Hyogo, Japan

Akira Adachi is an Associate Principal Engineer at Toyo Engineering Corporation in Narashino, Japan. He specializes in field troubleshooting of machinery problems as well as plant engineering studies including rotordynamic analysis, water hammer analysis, pulsation analysis, gas dynamic simulation, and CFD. Prior to current assignment, he had worked in various applications of rotating machineries during EPC projects of chemical, petrochemical, natural gas, and refinery plants. He received B.S. in Aeronautical Engineering from Nagoya University (1995) and M.S. in Mechanical Engineering from Stanford University (1996). He is a registered Professional Engineer in the State of Washington, and is also certified as Category IV Vibration Analyst.

Yoshitaka Baba is a Senior Manager of Advanced Technology Development Section in Technology Planning Department for the Machinery Business at Kobe Steel, Ltd. (KOBELCO), in Takasago, Japan. He is a specialist of rotordynamics, hydrodynamic bearings, and mechanical vibration. He has over 25 years of experience in research and development of centrifugal compressors, radial expanders, and other industrial machinery.
Mr. Baba has a BS and MS degree in Mechanical Engineering from Tohoku University.

ABSTRACT

Startup transients of both torsional and lateral vibration behaviors of an integrally geared centrifugal compressor driven by a synchronous motor are examined by transient torsional-lateral coupled analyses, and the numerical calculation results are evaluated using the field measurements as a benchmark. Since linear bearing coefficients are employed in the numerical simulation instead of more sophisticated nonlinear bearing model, bilinear stiffness is additionally considered to reflect the effects of the rotor confinement within the bearing clearance. Moreover, temporary teeth separation of the gear meshing and engagement at the backside during torque reversal is also considered in the numerical calculation. The transient lateral vibration behavior of the pinion rotor during the synchronous motor's startup is successfully replicated. Both (a) bilinear stiffness of the pinion rotor bearings due to rotor restraint within the bearing clearance, and (b) effect of temporary teeth separation within the backlash and engagement at the backside because of torque reversal, are found to strongly influence the numerical predictions.

INTRODUCTION

Machinery trains driven by synchronous motors can suffer from serious mechanical failures by large torque oscillation due to torsional resonance during the motor startup, unless the system is properly evaluated and designed (Corbo and Cook (2000)). Large torsional vibration occurs in such trains because synchronous motors, if not soft started by VFD (Variable Frequency Drive), generate torque oscillation during the acceleration with speed dependent excitation frequency that varies from 120Hz (or 100Hz in case of 50Hz line frequency) at the standstill to 0Hz when reaching the synchronous speed. As such, at some point during the motor acceleration, the excitation frequency coincides with the first torsional natural frequency (or possibly with the second followed by the first torsional

natural frequency) of the train, hence occurrence of torsional resonance is inevitable during a synchronous motor's startup.

In a geared train, such as a centrifugal compressor train driven by a synchronous motor via a speed increasing gear, large *lateral* vibration can also take place at the pinion rotor during the startup, because torque is converted to lateral force at the gear by torsional-lateral coupling mechanism which causes lateral vibration of the pinion rotor as a result of the torque oscillation (Iannuzzelli and Elward (1984)).

The transient *torsional* vibration occurrence in a train with a synchronous motor is well studied / documented and the evaluation methodologies are thoroughly established (Szenasi and von Nimitz (1978), Mruk (1978), Chen et al. (1983), Jackson and Leader (1983), Wachel and Szenasi (1993), Chen (1995), Corbo and Cook (2000), Yeiser et al. (2006)). On the other hand, the studies of the transient *lateral* vibration in such train are still underdeveloped and limited to either a qualitative discussion or a case with relatively small lateral displacements. In other words, systematic methodologies to enable quantitative evaluation of excessive *lateral* vibration occurrence are largely absent. Consequently, predictions of startup lateral vibration behavior of geared trains are primarily achieved only through empirical estimations, even though they are essential information in properly designing and evaluating machinery trains.

As an attempt to fill such gap, in this paper, startup transients of both torsional and lateral vibration behaviors of an integrally geared centrifugal compressor driven by a synchronous motor are examined in detail. Results of several numerical simulations by transient torsional-lateral coupled analyses with different degrees of modeling complexities are evaluated using the field measurement results as a benchmark. In this manner, effects of each numerical simulation assumption onto the calculation results are investigated to achieve adequate evaluation of the startup lateral vibration behavior of a geared train driven by a synchronous motor.

MOTIVATIONS BEHIND THIS STUDY

As reported at the TPS2020 by Adachi and Oba (2020), an integrally geared compressor driven by a synchronous motor suffered from a serious mechanical damage due to large startup torque oscillation. To counteract the problem, a controlled slip clutch was adopted to maintain the transmitted torque within the desired level. The clutch was successful in reducing the peak startup torque to one-third compared to prior to the clutch application, and the torsional failure problem was well rectified.

The train consisted of an integrally geared centrifugal compressor with three stages compression and a 7,500kW (10,000hp), four poles, salient pole synchronous motor which was across-the-line started without VFD at 50Hz line frequency. The compressor's bull gear and pinions were of single helical type. The rated speeds were 1,500rpm for the motor and the bull gear, 9,239rpm for the first / second stages pinion, and 15,635rpm for the third stage pinion. The bull gear rotor was connected to the synchronous motor via a spacer type diaphragm coupling, where the clutch was eventually applied on the motor side hub. (Figure 1 and Figure 2)

During the initial (i.e. prior to the clutch application) startup, in addition to the mechanical damage, very high lateral vibration in excess of 0.4mm(p-p) (16mils(p-p)) was also observed at the pinion rotor of the compressor's first & second stages. Nevertheless, observation of high lateral vibration was not unforeseen at the pinion rotor, because the gear meshing converts the transmitted torque to lateral force. Since the pinion lateral vibration was essentially caused by the excitation force due to torsional oscillation, it was logical to expect the lateral vibration amplitude to decrease according to the reduction of the torsional oscillation. As such, the lateral vibration level was anticipated to greatly improve by the clutch application.

Against such optimistic expectation, however, the clutch application did not significantly improve the lateral vibration level (Figure 3), even though it successfully reduced the peak torque to one-third as intended (Figure 4). In other words, startup lateral vibration amplitude of the pinion rotor was totally nonproportional to the transmitted torque oscillation magnitude. At this point, it was evident that no simple remedy existed to rectify the pinion rotor's lateral vibration level during startup. The startup lateral vibration was therefore mitigated by implementing a trip bypass with a timer for the pinion rotor's lateral vibration high-high trip function, i.e. trip function of the pinion high lateral vibration was programmed to be disabled for a predetermined time interval that covered the entirety of the motor acceleration duration.

The fact that the lateral vibration amplitude exhibited strong nonlinearity was nevertheless disconcerting, hence further studies which enable quantitative estimation of the startup lateral vibration behavior during the design phase were judged necessary.

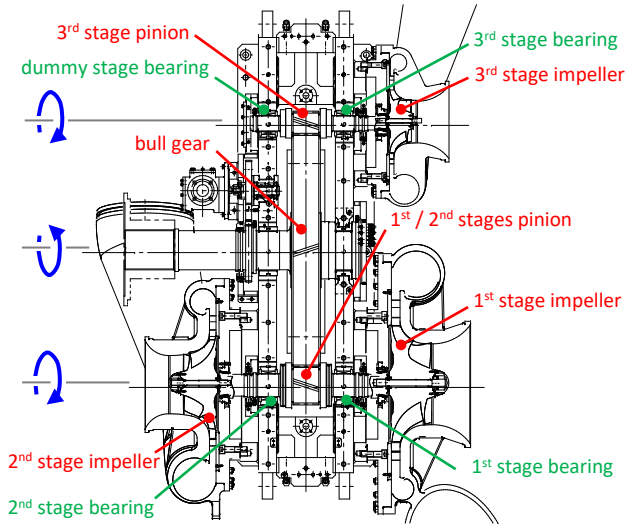

Figure 1. Cross Section of Integrally Geared Compressor

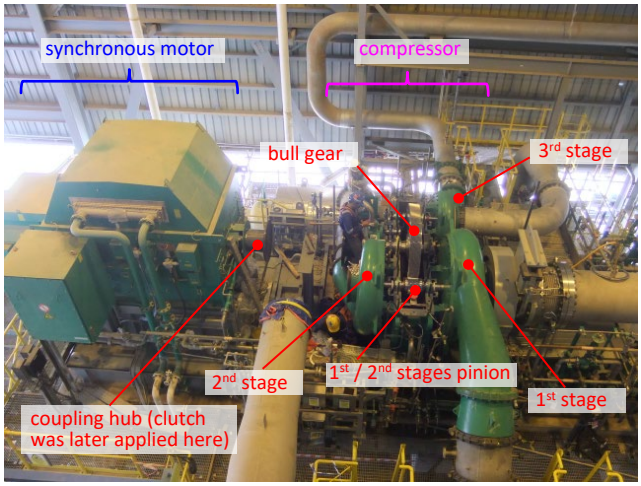

Figure 2. Train Overview (Partially Disassembled for Inspection)

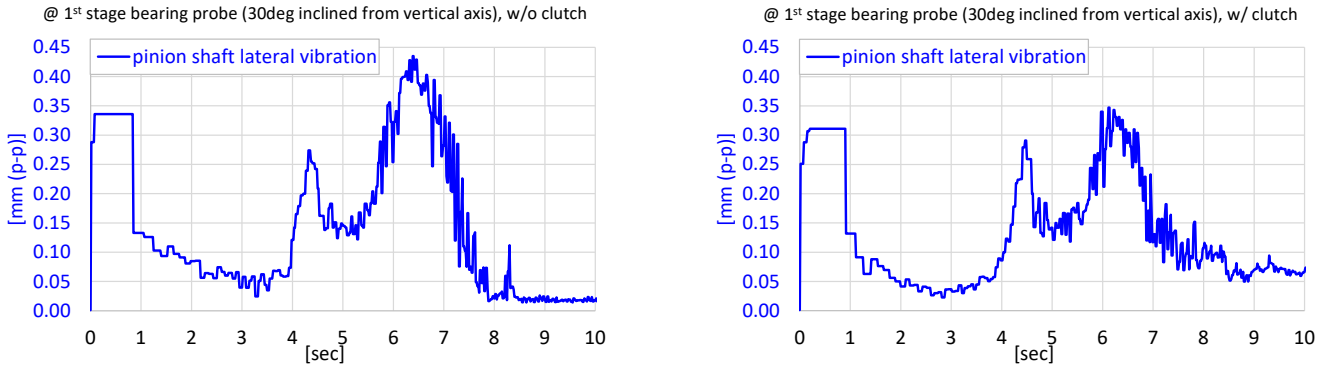

Figure 3. Lateral Vibration Transients Measured by Data Acquisition System (Left: without Clutch, Right: with Clutch)

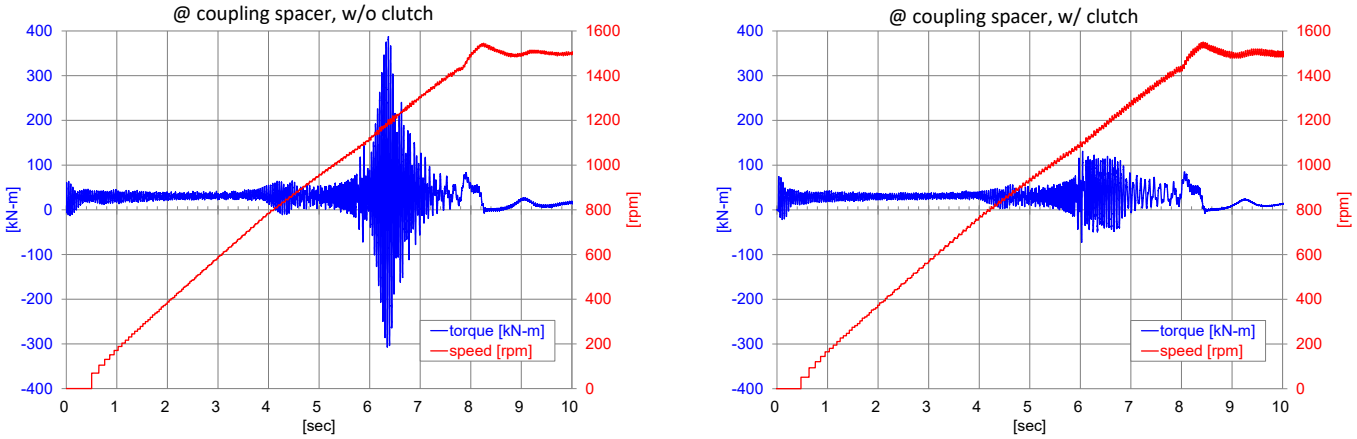

Figure 4. Measured Transmitted Torque and Rotational Speed (Left: without Clutch, Right: with Clutch)

MECHANISM OF TORSIONAL RESONANCE DURING SYNCHRONOUS MOTOR STARTUP

Many synchronous motors are self-starting with the principles of induction motors by utilizing damping bars (damper windings) as conductor bars. Generated torque in this manner is however not identical to that of ordinary squirrel cage induction motors, and the magnitude of the instantaneous torque during a synchronous motor's startup varies depending on the rotor position relative to the rotating magnetic field (Oscarson et al. (1954)). This is because of the following reasons:

- Unlike a squirrel cage induction motor, rotor of a synchronous motor is circumferentially anisotropic with poles and inter-pole spaces (Figure 5)
- Instantaneous starting torque is greater when the magnetic flux generated at the stator passes the rotor poles

- Less torque is developed when the magnetic flux passes the inter-pole spaces

In this way, generation of startup torque oscillation is unavoidable in a synchronous motor, unless it is soft started utilizing VFD.

The frequency of the torque oscillation decreases from either 120 Hz (in case of 60Hz line frequency) or 100Hz (in case of 50Hz line frequency) at standstill to 0 Hz at synchronous speed, and this occurs irrespective to the motor poles number. More specifically, the torque oscillation occurs at twice the slip frequency (slip frequency = motor slip × line frequency). This is because:

- Torque amplitude increases whenever the magnetic flux generated at the stator is at the rotor poles, and it decreases when the magnetic flux is at the inter-pole spaces → In each relative revolution of the magnetic field with respect to the rotor, torque amplitude experiences increase (and decrease) at the rate of the motor poles number
- Relative rotational speed of the magnetic field with respect to the rotor is expressed as the motor's synchronous speed multiplied by the motor slip, while the motor's synchronous speed is expressed as the line frequency divided by one-half of the number of motor poles
- The frequency of the generated torque oscillation is therefore expressed as:
  (relative rotational speed of the magnetic field with respect to the rotor) × (number of motor poles)
  = [{(line frequency) / (number of motor poles / 2)} × (motor slip)] × (number of motor poles)
  = 2 × (line frequency) × (motor slip)

Since a majority of machinery trains have the first torsional natural frequency below 30Hz (which is certainly below twice the line frequency), at some point during motor acceleration, oscillating torque frequency coincides with the first torsional natural frequency of the train (For trains with the second torsional natural frequency below twice the line frequency, oscillating torque frequency firstly coincides with the second torsional natural frequency, and then with the first torsional natural frequency). Occurrence of torsional resonance is therefore unavoidable during startup of a train driven by a synchronous motor. (Figure 6)

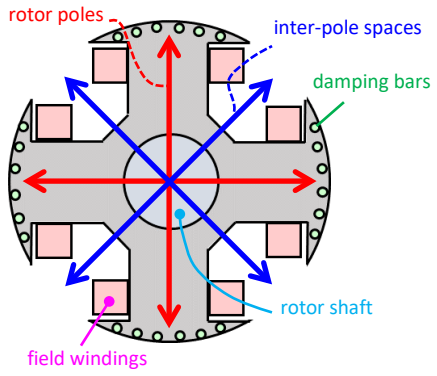

Figure 5. Rotor of Salient Pole Synchronous Motor

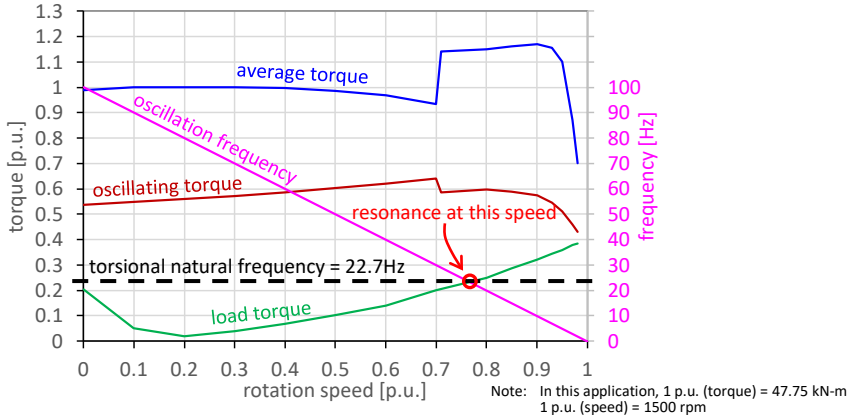

Figure 6. Startup Torque Characteristics of Synchronous Motor

TORSIONAL-LATERAL COUPLING

Lateral and torsional vibrations of a rotor system are normally considered independent of one another. In a geared train, however, coupling can occur between the lateral and torsional vibrations, i.e. torsional motion affects lateral motion, and vice versa (Figure 7). Pinion rotor is usually the most susceptible to such coupling mechanism, because it is typically lighter and slenderer compared to the bull gear rotor, hence its lateral and/or torsional motion can be more easily influenced.

In a synchronous motor driven geared train, large lateral vibration often occurs at the pinion rotor during startup due to torsional-lateral coupling mechanism, because generation of large torsional vibration is inevitable by a torsional resonance in such train as discussed in the previous section.

To examine the torsional and lateral vibrational behavior in such system, torsional-lateral coupled analysis can be employed (Iannuzzelli and Elward (1984), Rao et al. (1998), Friswell et al. (2010), Cao et al. (2015)). By using the coordinate system as in Figure 8, the meshing forces between the bull gear and the pinion are represented by the teeth in contact with a mesh stiffness which acts along the pressure line, along which the bull gear tooth moves the distance of $(x_b \sin\theta + y_b \cos\theta + r_b \varphi_b)$ while the pinion tooth moves the distance of $(x_p \sin\theta + y_p \cos\theta - r_p \varphi_p)$. The associated forces are then expressed as in Equation (1) according to Rao et al. (1998) and Friswell et al. (2010). From these expressions, coupling between the lateral and torsional motions is apparent, as the expressions for the lateral forces ($F_{x,b}$, $F_{y,b}$, $F_{x,p}$, $F_{y,p}$) involve the torsional displacements (φ_b and φ_p) and the expressions for the torsional forces (T_b and T_p) involve the lateral displacements (x_b, y_b, x_p, y_p).

In this study, linear meshing stiffness k_g of 1.92×10^9N/m (1.10×10^7lbf/in) is used as per the formulation in API TR684-1 (2019), while no mesh damping is considered in the numerical model.

$$\left.\begin{aligned}
F_{x,b} &= -k_g sin\theta\left[(sin\theta)x_b + (cos\theta)y_b - (sin\theta)x_p - (cos\theta)y_p + r_b\,\varphi_b + r_p\,\varphi_p\right]\\
F_{y,b} &= -k_g cos\theta\left[(sin\theta)x_b + (cos\theta)y_b - (sin\theta)x_p - (cos\theta)y_p + r_b\,\varphi_b + r_p\,\varphi_p\right]\\
F_{x,p} &= -k_g sin\theta\left[-(sin\theta)x_b - (cos\theta)y_b + (sin\theta)x_p + (cos\theta)y_p - r_b\,\varphi_b - r_p\,\varphi_p\right]\\
F_{y,p} &= -k_g cos\theta\left[-(sin\theta)x_b - (cos\theta)y_b + (sin\theta)x_p + (cos\theta)y_p - r_b\,\varphi_b - r_p\,\varphi_p\right]\\
T_b &= -k_g r_b\left[(sin\theta)x_b + (cos\theta)y_b - (sin\theta)x_p - (cos\theta)y_p + r_b\,\varphi_b + r_p\,\varphi_p\right]\\
T_p &= -k_g r_p\left[(sin\theta)x_b + (cos\theta)y_b - (sin\theta)x_p - (cos\theta)y_p + r_b\,\varphi_b + r_p\,\varphi_p\right]
\end{aligned}\right\} \quad (1)$$

where;

$F_{x\ or\ y,b}$	=	Lateral force onto bull gear, N (lbf)
$F_{x\ or\ y,p}$	=	Lateral force onto pinion, N (lbf)
T_b	=	Torque onto bull gear, $N\text{-}m$ $(in\text{-}lbf)$
T_p	=	Torque onto pinion, $N\text{-}m$ $(in\text{-}lbf)$
θ	=	Transverse pressure angle, rad (rad)
$x_b\ or\ y_b$	=	Lateral displacement of bull gear, m (in)
$x_p\ or\ y_p$	=	Lateral displacement of pinion, m (in)
φ_b	=	Torsional displacement of bull gear, rad (rad)
φ_p	=	Torsional displacement of pinion, rad (rad)
k_g	=	Mesh stiffness, N/m (lbf/in)
r_b	=	Base radius of bull gear, m (in)
r_p	=	Base radius of pinion, m (in)

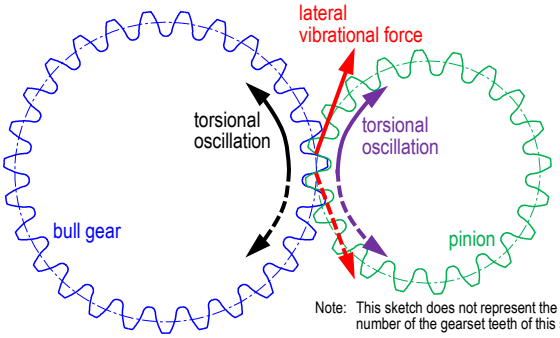

Figure 7. Conceptual Sketch of Torsional-Lateral Vibration Coupling

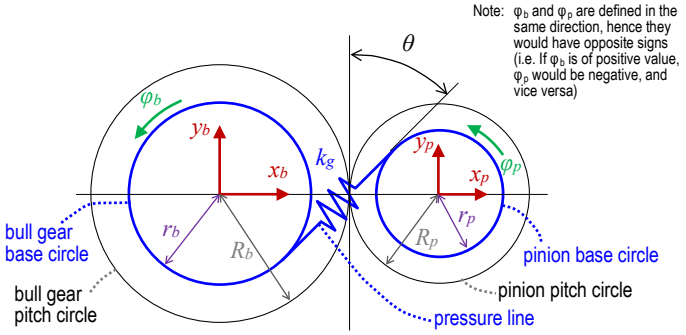

Figure 8. Coordinates for Torsional-Lateral Coupled Analysis

MODELING CONSIDERATIONS

In order to numerically simulate the transient behavior of the pinion rotor's lateral vibration, adequate modeling with accurate representations of the actual mechanical system is essential. Several modeling considerations are employed in this study in addition to the torsional-lateral coupling mechanism discussed above.

Shaft Modeling

In carrying out the analysis, accurate representation of the entire rotor system in the analytical model is essential (Corbo and Cook (2000), Wang et al. (2012)). Complex behaviors of the lateral and torsional motions of the shaft system are examined using the numerical simulation model that reflects the entire shaft string (Figure 9). The calculated first torsional natural frequency based on the torsional-lateral coupled analysis is 22.7Hz (Figure 10), which agrees well with the field measurement result using strain gauges.

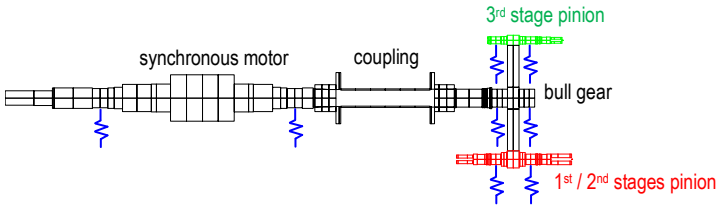

Figure 9. Shaft Model for Numerical Simulation

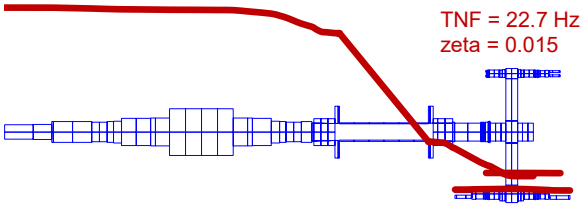

Figure 10. Calculated First Torsional Mode

Bearing Coefficients

In this study, bearing reaction forces are assumed linear with respect to the shaft displacement, i.e. bearing reaction forces are modeled by linear functions of the shaft lateral displacements and velocities, whose stiffness and damping coefficients only depend on the shaft rotational speed. While this is a normally employed approach in a majority of traditional lateral vibration studies (e.g. most unbalance response analyses employ such assumption), it may not be an exactly precise representation of the bearing reaction forces for the study of this paper, because the linear load-displacement relationship is only valid at small dynamic displacements from the rotor equilibrium position, while large lateral displacements can occur during the peak torque oscillation in this study as will be shown in the following sections. Since the lateral displacements would actually deviate from the small amount inherently assumed in the derivations of linear bearing model, more rigorous nonlinear models would be desirable.

Nevertheless, linear models often provide acceptable predictions for the behavior of real systems. Additionally, while some nonlinear models do exist for certain types of fluid film bearings, in particular for the fixed geometry sleeve bearings, such as those used for the study of oil whirl and whip by Adiletta et al. (1996), developing an appropriate nonlinear model for a tilting pad bearing can be challenging due to its geometrical complexities as well as its pads' movability around the pivots. Nonlinear modeling for tilting pad bearing forces requires to solve the pressure profile on each pad with the pivot effects and reflecting the lubricant film thickness, which needs to be updated at each time step of the transient analysis (Cao et al. (2013), Cao et al. (2015)). As such, reflecting these nonlinearities in the numerical model can make the transient calculation extremely time consuming due to being computationally intense and demanding, which would be burdensome in the course of a normal engineering evaluation (which is the main application this study is aiming for).

For these reasons, in this study, bearing reaction forces are intentionally simplified assuming linearity with respect to the shaft displacement.

The compressor's pinion rotor in this study has tilting pad (with 5 pads) journal bearings. Employed bearing coefficients (stiffness and damping coefficients) are shown in Figure 11, which are derived by numerically solving the pressure equation with the energy and the elasticity equations. Since the torque transmission from the bull gear to the pinion acts as additional bearing load due to torsional-lateral coupling mechanism along with the gravity force, such load is considered in the derivation of bearing coefficients, using the load corresponding to the beginning of acceleration for the entire speed range.

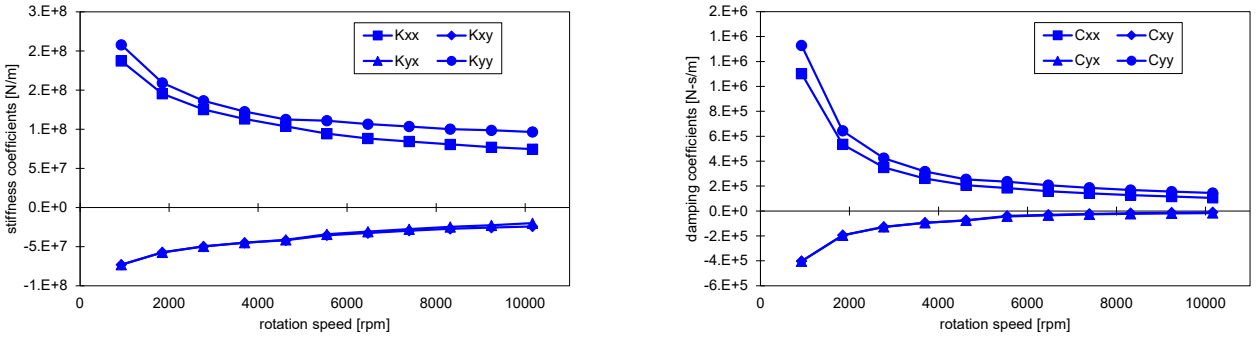

Figure 11. Journal Bearing Coefficients of 1st / 2nd Stages Pinion Rotor (Left: Stiffness Coefficients, Right: Damping Coefficients)

Shaft Movement Constraint (Bilinear Stiffness Due to Rotor to Stator Contact)

As discussed, large lateral displacements of the pinion rotor can occur during the peak torque oscillation due to torsional-lateral coupling. Displacements of the pinion rotor can be such large to cause the shaft to contact the journal bearing inner surface, i.e. rotor to stator contact occurs at the journal bearing, which practically restricts the shaft movement within the bearing clearance.

Since the assumed bearing reaction forces do not reflect such effect and the simplified linear coefficients are instead employed, the effect due to confinement within the bearing clearance onto the pinion rotor's lateral motion needs to be additionally considered. To do so, bilinear stiffness is assumed in the bearing model, i.e. shaft movement beyond the bearing clearance would be constrained by the bilinear spring stiffness that acts in addition to the linear bearing coefficients discussed in the previous section (Figure 12).

Force due to this effect can be expressed as in Equation (2) (Ehrich (1988), Friswell et al. (2010)). The initial location of the shaft center (δ in Figure 13) is assumed to be zero in this study. In other words, the pinion rotor is initially positioned at the stator center during the standstill in the numerical model. In this study, bilinear stiffness k_{BL} of 5×10^9N/m (2.9×10^7lbf/in) is applied.

$$F_{x,BL} = \begin{cases} 0 & for \quad r \le r_0 \\ -k_{BL}(r - r_0)x_p/r & for \quad r > r_0 \end{cases}$$

$$F_{y,BL} = \begin{cases} 0 & for \quad r \le r_0 \\ -k_{BL}(r - r_0)(y_p - \delta)/r & for \quad r > r_0 \end{cases} \qquad (2)$$

where;

$F_{x\ or\ y,BL} =$	Contact force due to bilinear stiffness, $N \quad (lbf)$
$k_{BL} =$	Bilinear stiffness, $N/m \quad (lbf/in)$
$r =$	Radial distance between stator center and pinion shaft center, $m \quad (in)$
$r_0 =$	Bearing radial clearance, $m \quad (in)$
$x_p\ or\ y_p =$	Lateral displacement of pinion, $m \quad (in)$
$\delta =$	Initial offset of pinion shaft center from stator center, $m \quad (in)$

While in the study of rub induced vibrations it is customary to consider both the radial force due to contact and the tangential force due to friction, in this study only the radial contact force is considered without the tangential frictional force. This is justifiable because the bearing pads, which are the only potential contacting surfaces, are lubricated by bearing oil so the frictional force would be negligible, if any.

Since the pads can tilt around the pivots, the clearance profile actually depends on the shaft circumferential position. Tilting pad journal bearing generally has a clearance profile of polygon shape, having the number of sides corresponding to the number of pads of the bearing. For example, in case of a tilting pad bearing with 5 pads, it has a clearance profile of pentagon shape (Figure 14). Moreover, because the contact force acts normal to the pentagon edges, the force direction is actually anisotropic, while the force in Equation (2) is always directed toward the stator center. Although such anisotropies of the clearance profile as well as of the contact force direction can be reflected into the numerical simulation model, in this study they are neglected for the sake of simplicity, and the bilinear stiffness is assumed to have no circumferential anisotropy, i.e. circular clearance profile is assumed.

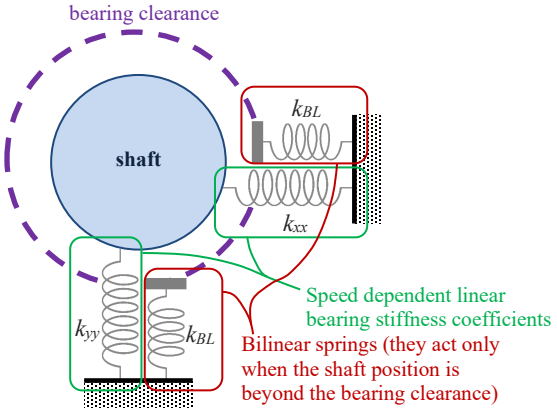

Figure 12. Conceptual Sketch of Bilinear Stiffness

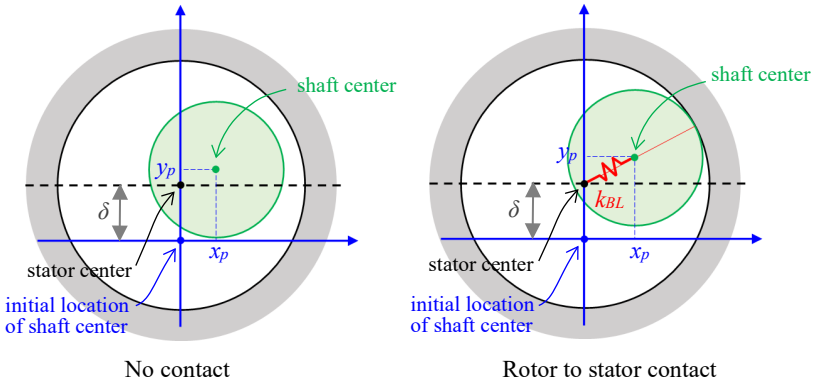

Figure 13. Coordinates for Bilinear Stiffness Force

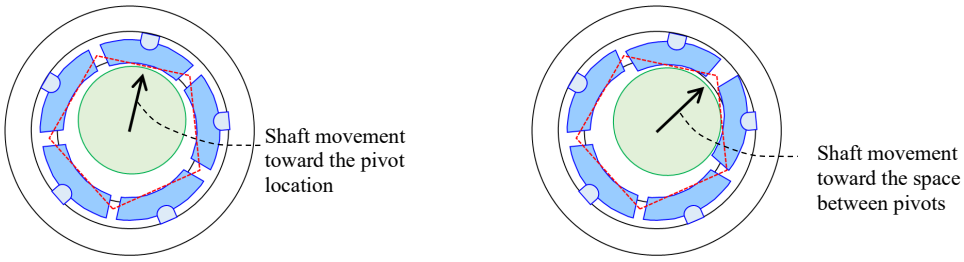

Figure 14. Clearance Profile of Tiling Pad Journal Bearing

Temporary Teeth Separation

During the peak torsional oscillation, torque reversal can occur, which makes the gear meshing temporarily separate within the backlash and eventually engage at the backside of the neighboring tooth. When this happens, either the meshing forces disappear or their direction of action alters. Teeth meshing can consequently be categorized into three conditions based on the teeth engagement (Figure 15); (a) meshing forces between the bull gear and the pinion act along the pressure line when the teeth are engaged in forward direction, (b) no

meshing force acts during the temporary teeth separation, (c) the pressure line along which the meshing forces act is different when the teeth are engaged at the backside. (See also Appendix A at the end of this paper for more detailed discussions on numerical formulations)

The torsional-lateral coupling forces can therefore be significantly affected by the teeth meshing condition. The effects of such temporary teeth separation and engagement at the backside onto the torsional-lateral coupled analysis results are investigated.

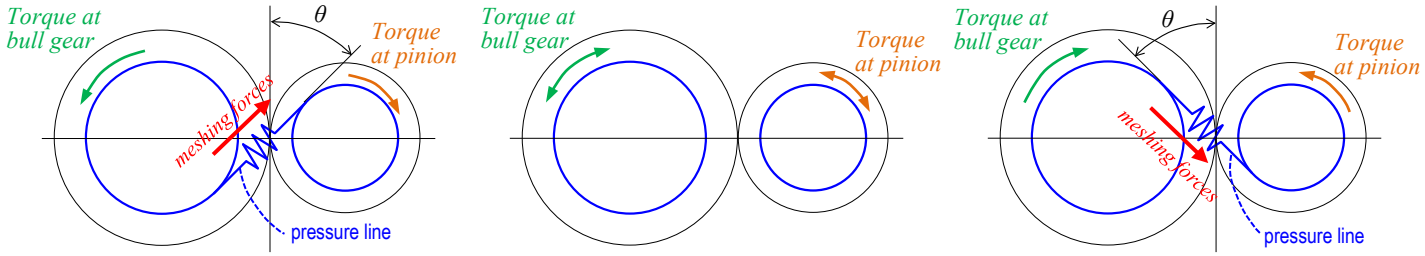

(a) Teeth engaged in forward direction (Meshing forces act along the pressure line)

(b) Teeth separated within backlash (No meshing force acts)

(c) Teeth engaged at the backside (Meshing forces act along different pressure line)

Figure 15. Effect of Teeth Separation onto Torsional-Lateral Coupled Forces

Voltage Drop and Motor Output Torque

During starting of an electric motor, significantly more current is pulled than the full load current if started across-the-line. Because of that, associated electrical system becomes heavily loaded and the components such as cables and transformers saturate, resulting in a temporary voltage drop. This in turn causes the motor starting torques (average torque as well as oscillating torque) to decrease.

Since the field measurements of this study were carried out while the plant was still under construction and was not fully operational, the short circuit capacity of the associated electrical system was different from the design considerations. Voltage droppage consequently slightly deviated from that assumed during the design phase. Motor starting torque reflecting the short circuit capacity under the actual plant condition at the field measurement timing is therefore considered in this study (Figure 16).

Once the motor reaches a speed close to the synchronous speed, typically above 95% of the synchronous speed, field excitation is applied and rotor is pulled into synchronization. The effect of synchronization is however not reflected in the numerical models, because major vibrational events take place well below the synchronization speed and it is therefore not of the main interest of this study, i.e. it does not alter the conclusion of this study irrespective of exclusion of this effect.

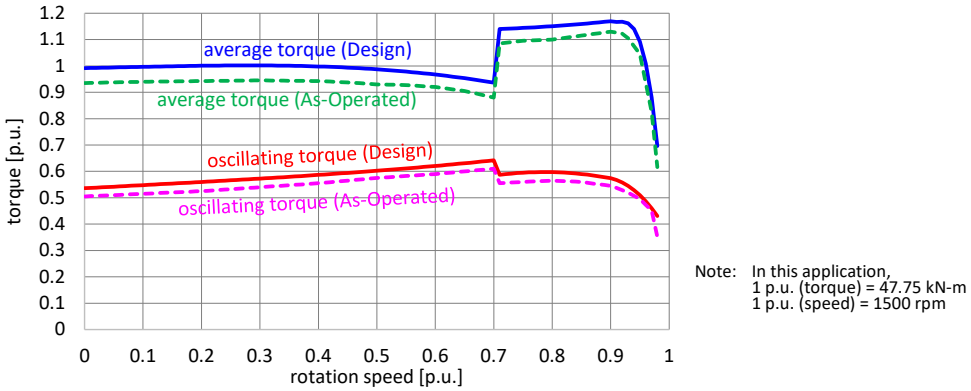

Figure 16. Motor Output Torque (Solid Line: Based on Design Condition, Dashed Line: Based on "As-Operated" Short Circuit Capacity)

Torsional Damping

The degree of available torsional damping directly affects the calculated torque oscillation magnitude that is closely related to the lateral vibration amplitude of the pinion rotor. As such, meticulous representation of the torsional damping is critical in obtaining accurate numerical simulation results (Corbo and Malanoski (1996), Corbo and Cook (2000), Wang et al. (2012), Pradetto and Baumann (2015), Sciancalepore et al. (2019)).

In torsional-lateral coupled analysis, damping due to bearing oil film acts as one of the major sources of torsional damping along with the structural damping of the entire shaft system including the coupling spacer. As such, when allocating generic damping ratio distributed throughout the shaft system it is important to properly account for the torsional damping effect due to the lateral damping by the bearing oil film. In other words, simply applying the identical structural damping matrices of the shaft system as in a pure torsional study could result in overestimation of the torsional damping effect, because the lateral damping due to bearing oil film also contributes to gain some torsional damping in a torsional-lateral coupled analysis. In this study, stiffness proportional torsional damping is assumed

throughout the shaft system which, together with the damping due to the bearing oil film, adds up to the overall critical damping of 1.5% for the first torsional mode of 22.7Hz, because the field strain gauge measurement during coasting down found the critical torsional damping of this machinery train as 1.5% (Adachi and Oba (2020)).

Unbalance Forces

Lateral forces due to residual unbalances are intentionally omitted in the numerical model, even though it is not difficult to reflect some unbalance forces in the calculation. This is due to several reasons; Since the actual distributions (axial distribution of each unbalance amount and its relative angular position) of residual unbalances are not exactly known, assuming such distribution may introduce uncertainties as well as the possibilities of manipulation. Moreover, the effect of unbalance forces onto the lateral vibrational amplitude may anyway be limited during the startup because the torsional-lateral coupled forces due to torsional oscillation are more pronounced, hence they are not essential in this study.

Controlled Slip Clutch

As shown in Figure 17, a controlled slip clutch consists of three main parts – conical sleeve (driving part), flange sleeve (driven part), and ring with safety mechanism (protection mechanism part). The clutch assembly is applied at the coupling hub on the motor shaft. In this clutch, torque is transmitted through a friction joint where the torque carrying capacity is precisely controlled by the hydraulic oil pressure imposed by the ring with safety mechanism. As long as the torque is within the predetermined setting value, it is fully transmitted to the driven part through static friction between two concentric sleeves (conical sleeve and flange sleeve). On the other hand, when the torque exceeds the preset value, the flange sleeve (driven part) slips against the conical sleeve (driving part) such that only the predetermined amount of torque is transmitted to the driven part through dynamic friction. In this way, the maximum transmitted torque is precisely controllable during any transients including synchronous motor's startup while unaffecting normal operation of the compressor train.

Because of such torque transmission mechanism, a controlled slip clutch inherently adds considerable amount of torsional damping (torsional energy dissipation through frictional force) during slippage, so the torque oscillation can be markedly reduced. Since slippage occurs only at the timing of significant torsional oscillation when the need for peak torque suppression is greatest, the clutch is a very effective remedy in reducing large transient torsional oscillation (Yeiser et al. (2006), Maier and Studley (2017), Adachi and Oba (2020)).

In the numerical simulation, controlled slip clutch is modeled in the following manner (Figure 18):

- As long as the transmitted torque across the clutch is within the slip setting value (125kN-m (92.2ft-klbf) in this study), the clutch is engaged and rigidly connects the driving and driven parts, i.e. torque is transmitted by static friction across the clutch
- When the transmitted torque across the clutch exceeds the slip setting value, slippage begins to occur
- During slippage, only 70% of the slip setting torque is transmitted to the driven part (70% because torque is transmitted by dynamic friction across the friction joint of the clutch)
- Slippage continues as long as the angular velocity of the driving part exceeds that of the driven part
- When the angular velocity of the driving part equals that of the driven part, slippage terminates, and the two parts act as rigid connection again

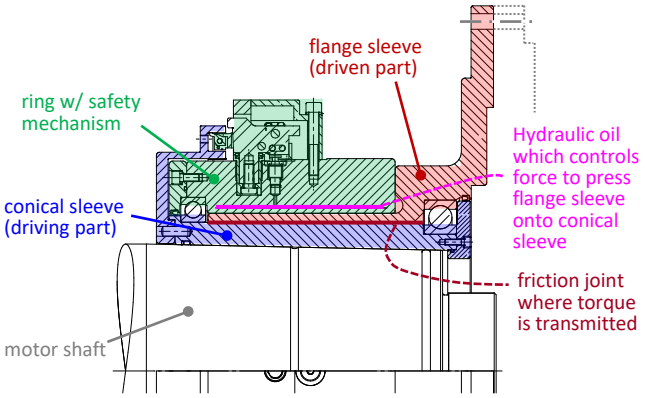

Figure 17. Cross Section of Controlled Slip Clutch

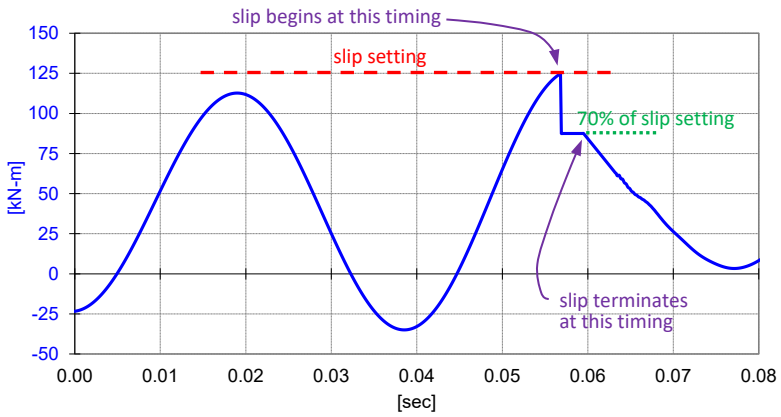

Figure 18. Torque Transmission Concept through Controlled Slip Clutch

EVALUATION OF NUMERICAL CALCULATION RESULTS

Startup transient behavior of the integrally geared centrifugal compressor train driven by the synchronous motor is investigated by torsional-lateral coupled analysis, and the numerical results are evaluated using the field measurement results as a benchmark. Modeling complexities are gradually added in the numerical simulation assumptions so as to confirm the effects of each modeling detail onto the

calculation results.

Field Measurement Results (Benchmark Data)

In the field, transient data of the transmitted torque, the rotational speed, and the lateral vibrations were concurrently gathered. The transmitted torque was measured by strain gauges applied at the coupling spacer, while the rotational speed was captured by optical pickup device with reflective marks at the rotor. The lateral vibrational data were collected utilizing a data logger connected to the output ports of the data acquisition system for the proximity sensors which were mounted adjacent to the pinion journal bearings.

Measured transmitted torque and speed are shown in Figure 4 of the previous section. Peak torque of 388kN-m (286ft-klbf) occurs at 6.4sec after motor energizing without the clutch. With the clutch, peak torque is suppressed to within 125kN-m (92.2ft-klbf). In other words, the clutch reduces the peak torque to one-third.

The torque transients of Figure 4 show small peaks at 4.0~4.6sec prior to the major peak amplitude occurrence at 6.0~7.0sec. The major torque oscillation at 6.0~7.0sec occurs at 23Hz, which is the first torsional natural frequency of the shaft system. This oscillation is due to the torque pulsation generation mechanism inherent in the startup of a synchronous motor discussed in the previous section. The torque oscillation during 4.0~4.6sec also dominantly occurs at 23Hz. However, this oscillation at 4.0~4.6sec cannot be due to the mechanism inherent in a synchronous motor, because the rotational speed during this period is only 800~900rpm, hence twice the slip frequency corresponds to 40~47Hz which is far away from 23Hz. These small torque peaks at 4.0~4.6sec are likely due to some unidentified disturbances, probably in the electrical feed system.

Measured lateral displacements at the pinion's first stage bearing probes are shown in Figure 19 (vertical direction) and Figure 20 (horizontal direction). Peak lateral displacements occur at the timing of the greatest torque transmission (6.0~7.0sec). Unlike the transmitted torque, however, the lateral vibration amplitudes do not significantly reduce by the clutch application, i.e. the maximum vertical vibration amplitude is 0.5mm(p-p) (20mils(p-p)) without the clutch, while it is 0.4mm(p-p) (16mils(p-p)) with the clutch.

Measured lateral vibration also shows small peaks at 4.0~4.6sec prior to the major peak amplitude occurrence at 6.0~7.0 sec. These small peaks at 4.0~4.6sec are due to the torque oscillation via torsional-lateral coupling mechanism.

Measured shaft vibration orbits are shown in Figure 21, which exhibit complex trajectories with abrupt changes in whirling motion. As expected, the vibration orbits are basically confined within the assumed bearing clearance limit indicated by the dotted line in orange color, which is based on the nominal diametrical clearance of 0.40mm (16mils). Its center is at the vertical location of 0.23mm (9mils). This is because the shaft location during the standstill condition is used for determining the zero position in this graph. Since the rotor's standstill position does not correspond to the bearing center, it is logical that the center of the clearance limit in Figure 21 is not at zero. Moreover, since the pinion bearings are aligned such as to position their centerline at the pinion shaft centerline when the gear teeth are engaged, the zero position can be further offset.

The arrows in Figure 21 contain the assumed timing when the teeth are temporarily separated. Since the teeth engagement condition was not directly measured, arrows in Figure 21 are drawn to contain the timing shortly after the torque transmission direction at the coupling spacer changes, because that is the likely moment when the teeth are temporarily separated. From these graphs, the teeth engagement condition as well as the change in torque transmission direction seem to significantly affect the occurrence of abrupt changes in orbital motion.

In Figure 22, detailed orbits are shown with segmented orbital motion based on the direction of the measured transmitted torque at the coupling spacer. These orbits show that the direction of trajectory changes each time the torque transmission condition is changed from positive to reverse or vice versa, which indicates that the teeth engagement condition can significantly affect the shaft orbital motion.

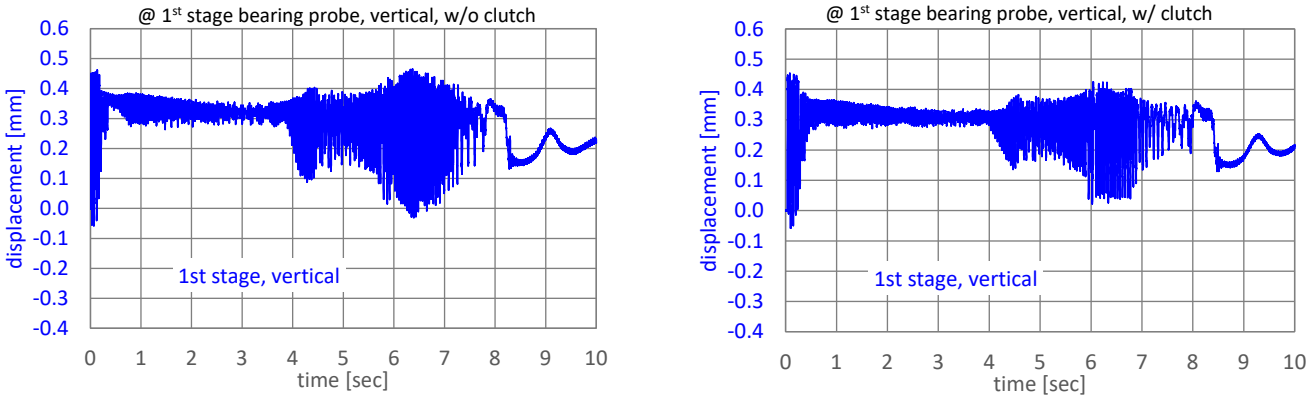

Figure 19. Measured Lateral Vibration Transients in Vertical Direction, Left: without Clutch, Right: with Clutch

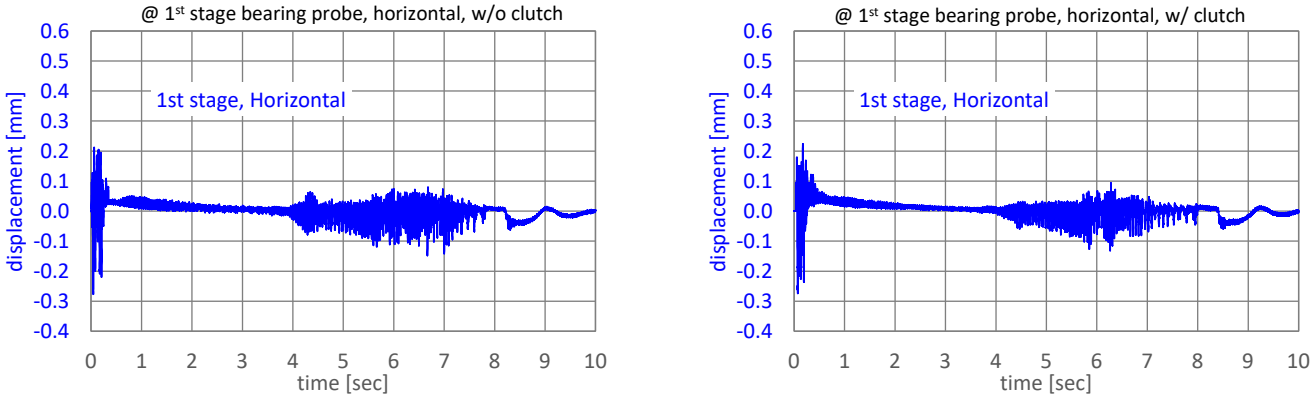

Figure 20. Measured Lateral Vibration Transients in Horizontal Direction, Left: without Clutch, Right: with Clutch

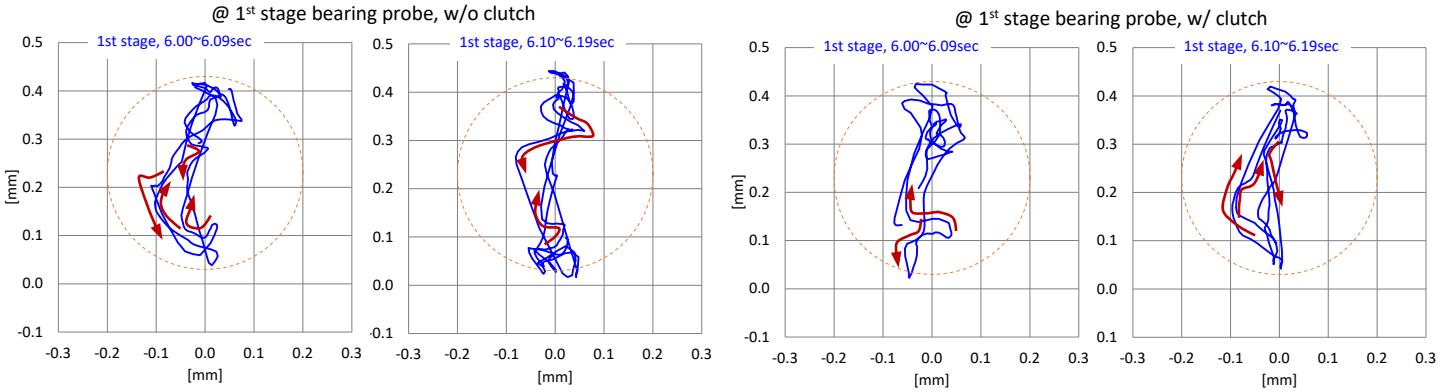

Figure 21. Measured Vibration Orbit, Left: without Clutch, Right: with Clutch

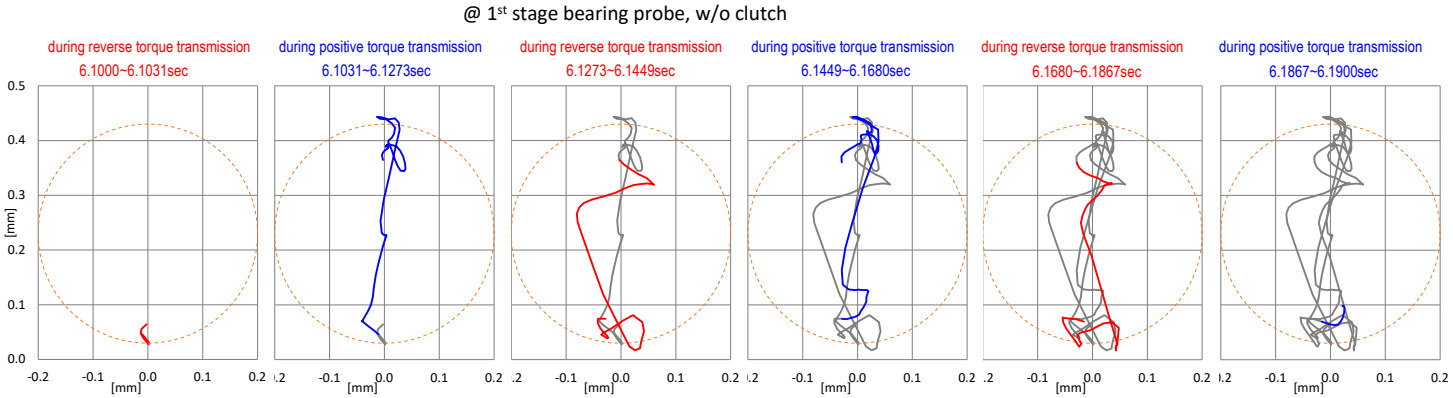

Figure 22. Detailed Trajectories of Measured Vibration Orbit without Clutch

Base Case Results (Neither Bilinear Stiffness nor Teeth Separation Considered)

Transient torsional-lateral coupled analysis results are shown in Figure 23 (transmitted torque), Figure 24 (lateral vibration in vertical direction) and Figure 25 (lateral vibration in horizontal direction), which consider the motor output torque characteristics reflecting the "as-operated" short circuit capacity, but neither the bilinear stiffness of the journal bearing nor the temporary teeth separation of the gear meshing is considered.

The torque transients of Figure 23 well replicate the measurement results of Figure 4, except that the small peaks at 4.0~4.6sec in the measurements are not captured in the numerical simulations. As discussed, this torque oscillation at 4.0~4.6sec is likely due to some disturbances, probably in the electrical feed system, which are not reflected in the numerical simulation model.

The amplitude of the lateral transients of Figure 24 and Figure 25 is basically proportional to the calculated transmitted torque amplitude, which is natural because the lateral vibration of the pinion rotor is essentially caused by the torque oscillation via torsional-lateral coupling mechanism. Consequently, the calculated peak lateral vibration amplitude is reduced to approximately one-third in case the

clutch is applied. In other words, the prediction of lateral vibrational behavior is totally unsatisfactory and cannot be applicable for any quantitative evaluation. This deviation is essentially attributable to neglecting either the bearing force nonlinearity or the bilinear stiffness which confines the pinion rotor's movement within the bearing clearance.

The numerical prediction for the lateral transients also fails to replicate the small peaks at 4.0~4.6sec of the measurement. This discrepancy is due to the deviation of transient torque prediction as discussed above.

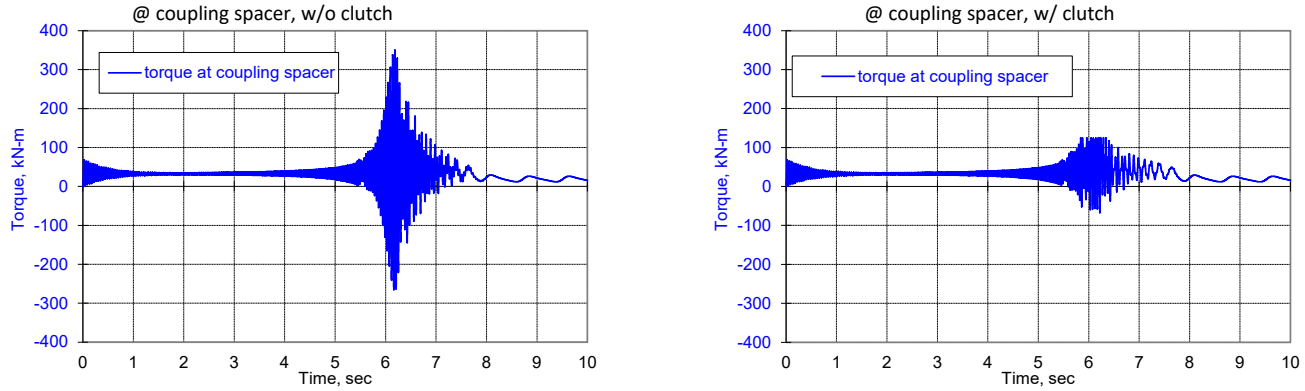

Figure 23. Calculated Torque Transients (Base Case), Left: without Clutch, Right: with Clutch

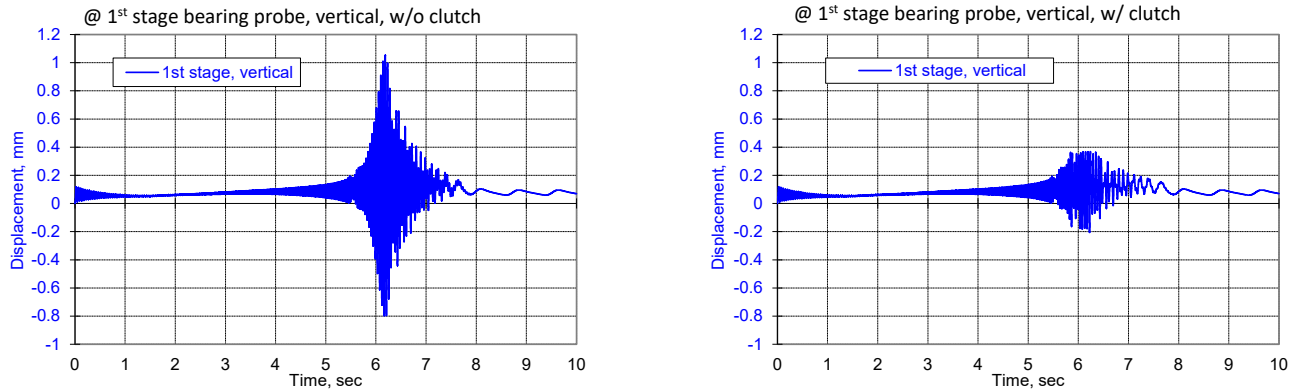

Figure 24. Calculated Lateral Vibration Transients in Vertical Direction (Base Case), Left: w/o Clutch, Right: w/ Clutch

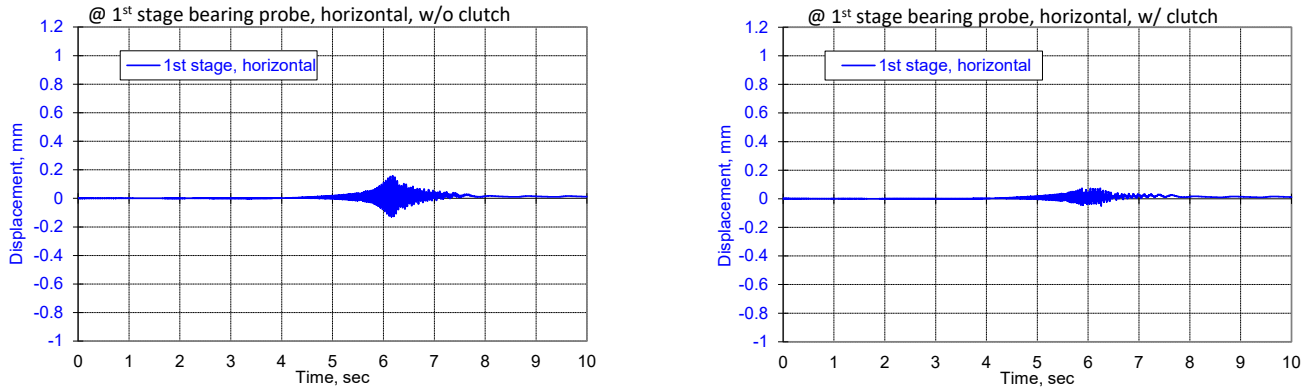

Figure 25. Calculated Lateral Vibration Transients in Horizontal Direction (Base Case), Left: w/o Clutch, Right: w/ Clutch

Refined Results with Bilinear Stiffness

Refined analysis results are shown in Figure 26 (lateral vibration in vertical direction), Figure 27 (lateral vibration in horizontal direction) and Figure 28 (shaft vibration orbit), which consider the motor output torque characteristics reflecting the "as-operated" short circuit capacity as well as the bilinear stiffness of the journal bearing but without the temporary teeth separation of the gear meshing. Since the calculated torque transients are almost identical to those of Base Case results in Figure 23, they are not shown here.

The lateral transients of Figure 26 and Figure 27 show the predictions for the pinion vibration reasonably replicate the measured vibrational transients of Figure 19 and Figure 20. The predicted peak vibration amplitudes (0.44mm(p-p) (17mils(p-p)) without clutch, 0.38mm(p-p) (15mils(p-p)) with clutch) quantitatively match those of the measurements. The major deviations are; (1) During the very

beginning of the acceleration at 0.0~0.5sec, the rotor is lifted up by 0.3~0.45mm (12~18mils) in the measurement, while the predicted lifting is merely 0.1mm (4mils), and during throughout the acceleration the rotor is lifted by approximately 0.3mm (12mils) in the measurement, while the lift in numerical prediction is merely 0.06~0.10mm (2~4mils). (2) At 4.0~4.6sec, small peaks are observed in the measurement, while the numerical prediction fails to capture these small peaks.

Prediction of the bearing reaction force at very low rotational speed is sometimes extremely poor, hence such deviation can be a contributor to the discrepancy in rotor lift. Moreover, when the motor is energized and the bull gear starts to rotate, the gear meshing between the pinion and the bull gear is abruptly engaged, which causes the pinion rotor lifted up. Since such effect due to abrupt teeth engagement is not reflected in the numerical model, this can be another contributing factor of the discrepancy.

On the other hand, the absence of the small peaks at 4.0~4.6sec in the numerical prediction is primarily due to not being able to accurately capture the torque transients during this period as discussed in the previous section.

Prediction of the shaft vibration orbits of Figure 28 shows that the shaft trajectory is basically confined within the bearing clearance indicated by the dotted line in orange color. The center of the bearing clearance limit is at the vertical location of 0.0mm (0mils) in Figure 28, while in Figure 21 (measured orbits) it is at 0.23mm (9mils). This difference is because (a) the numerical model does not reflect the abrupt engagement of the gearset teeth upon motor energizing, and they are instead assumed to have been engaged since the very beginning of the calculation, while (b) the measured results include the effects due to the abrupt engagement of the gearset teeth upon motor energizing. Consequently, the effects of rotor lift due to abrupt teeth engagement do not appear in the numerical calculation, while they do in the measurement. Another reason is because the zero position is defined differently; it is defined by the bearing clearance center in the numerical model, while the rotor position during standstill is used in the measurement results.

It should be noted that the complex trajectories with abrupt changes in whirling motion as shown in the measured orbits of Figure 21 are not exactly replicated in the numerical prediction of Figure 28, and the predicted orbits exhibit mostly straight trajectories except at the bearing clearance limit. In other words, the predicted orbits of this numerical simulation case are overly smooth.

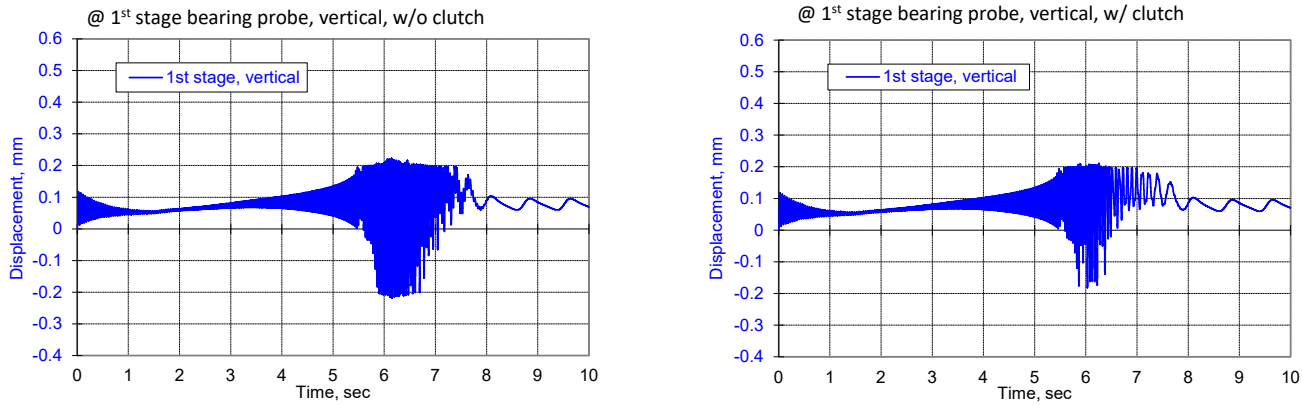

Figure 26. Calculated Lateral Vibration Transients in Vertical Direction (w/ Bilinear Stiffness), Left: w/o Clutch, Right: w/ Clutch

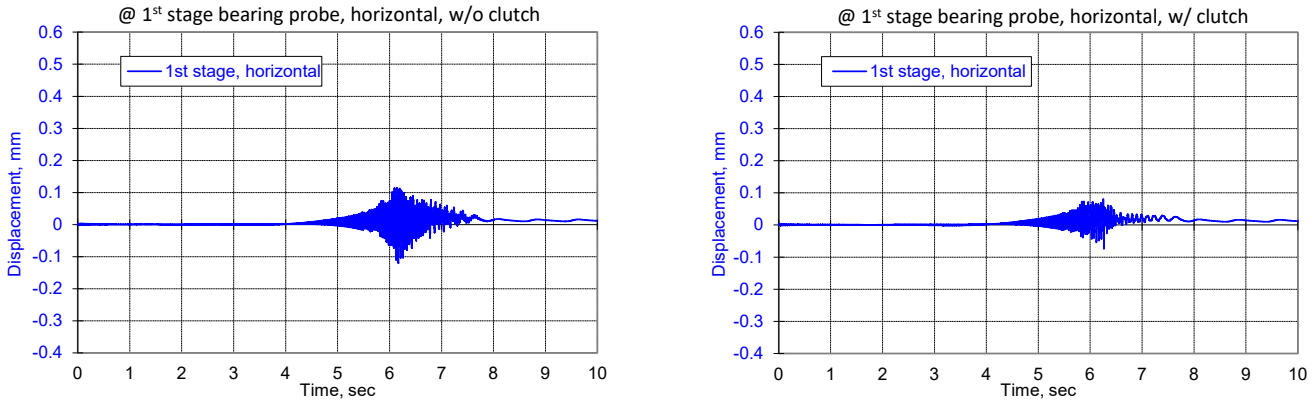

Figure 27. Calculated Lateral Vibration Transients in Horizontal Direction (w/ Bilinear Stiffness), Left: w/o Clutch, Right: w/ Clutch

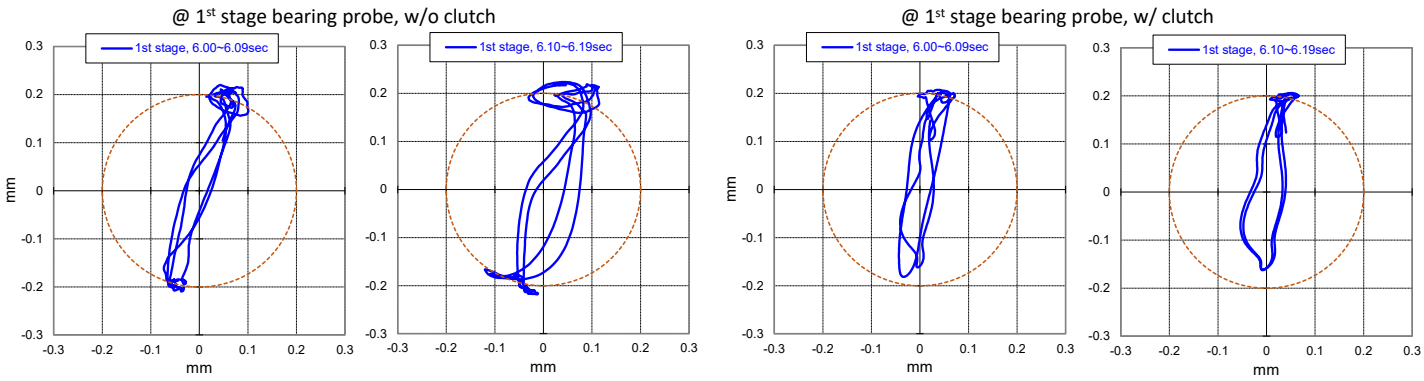

Figure 28. Calculated Shaft Vibration Orbit (w/ Bilinear Stiffness), Left: w/o Clutch, Right: w/ Clutch

Results with Further Refinement That Reflects Temporary Teeth Separation

Numerical calculation results with further refinement are shown in Figure 29 (lateral vibration in vertical direction), Figure 30 (lateral vibration in horizontal direction), and Figures 31 & 32 (shaft vibration orbit), which consider the motor output torque characteristics reflecting the "as-operated" short circuit capacity as well as the bilinear stiffness of the journal bearing and the temporary teeth separation of the gear meshing. Since the calculated torque transients are very similar to those of Base Case result in Figure 23, they are not shown here.

The lateral transients of Figure 29 and Figure 30 show the prediction for the pinion vibration reasonably replicates the measured vibrational transients of Figure 19 and Figure 20. The predicted peak vibration amplitudes of 0.49mm(p-p) (19mils(p-p)) without clutch and 0.40 mm(p-p) (16 mils(p-p)) with clutch are quantitatively satisfactory, closely matching the measurement results. The major deviations are once again (1) rotor lifting during the very beginning of the acceleration at 0.0~0.5sec as well as throughout the acceleration, which is considerably smaller compared to the measurement, and (2) vibration amplitude at 4.0~4.6sec, when small peaks are observed in the measurement. Additionally, in this case, (3) predicted transient vibrational amplitude in horizontal direction without clutch, which tends to be larger than the measurement, is another factor of deviation.

Predicted shaft vibration orbits of Figure 31 show more complex trajectories with abrupt changes in whirling motion compared to those in Figure 28, which indicate that the measured orbits of Figure 21 could have been influenced by the temporary teeth separation and engagement at the backside teeth that can strongly affect the force direction as well as the absence of torsional-lateral coupling force. The arrows in Figure 31 contain the timing when the teeth are temporarily separated in the numerical calculation that affects the direction of orbital trajectory. To illustrate how the torque direction and the teeth engagement condition affect the orbital trajectory, Figure 32 shows the detailed orbits with segmented orbital motion based on the direction of the calculated transmitted torque at the coupling spacer as well as the teeth engagement condition. These detailed orbits confirm that the direction of trajectory changes each time the teeth are temporarily separated and reengaged after temporary separation.

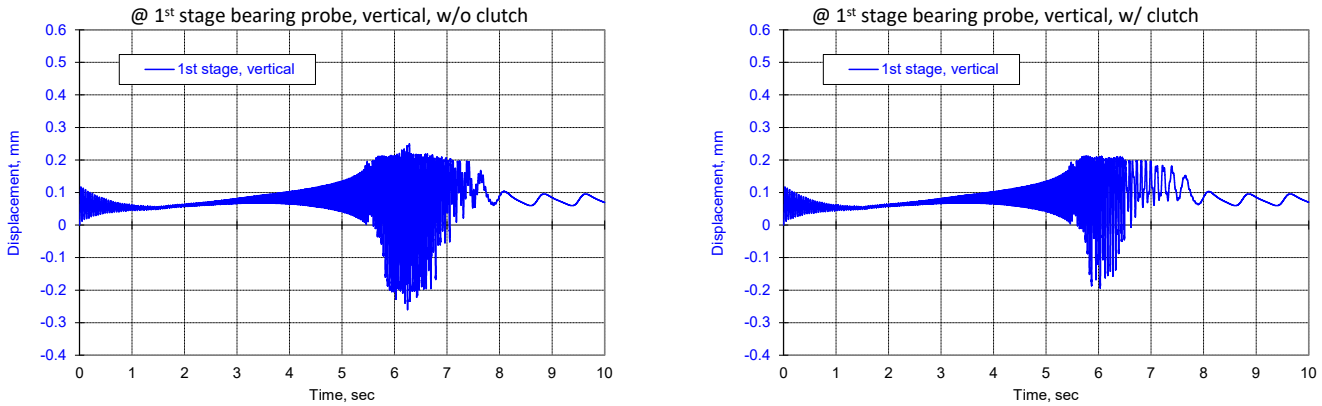

Figure 29. Calculated Lateral Vibration Transients in Vertical Direction (w/ Teeth Separation), Left: w/o Clutch, Right: w/ Clutch

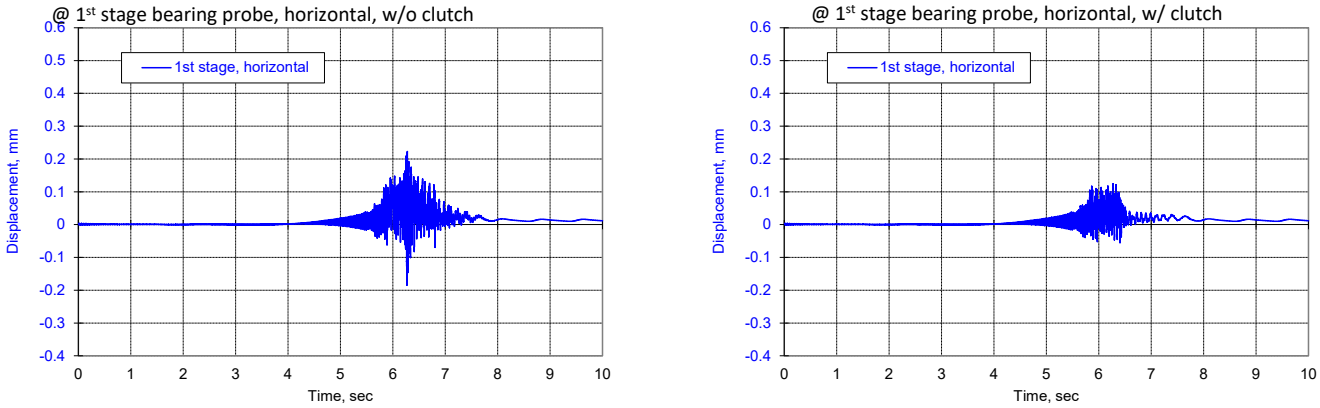

Figure 30. Calculated Lateral Vibration Transients in Horizontal Direction (w/ Teeth Separation), Left: w/o Clutch, Right: w/ Clutch

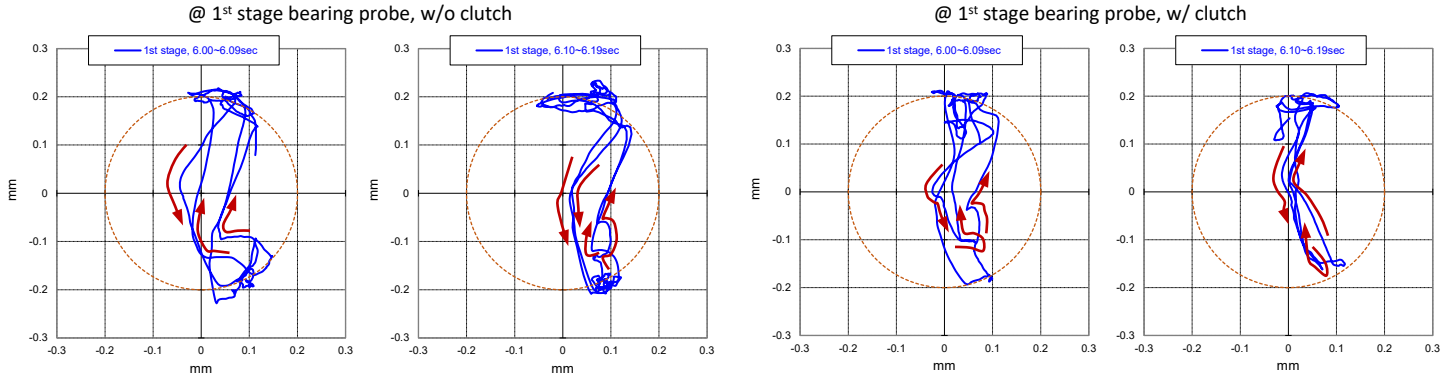

Figure 31. Calculated Shaft Vibration Orbit (Teeth Separation is Considered), Left: without Clutch, Right: with Clutch

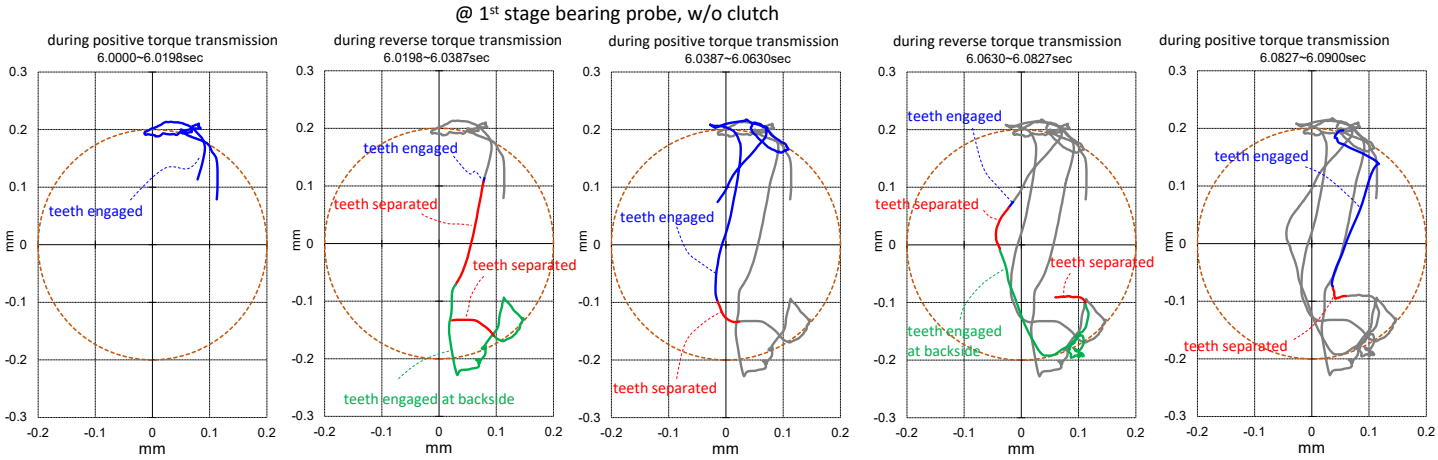

Figure 32. Detailed Trajectories of Calculated Shaft Vibration Orbit without Clutch (Teeth Separation is Considered)

CONCLUSIONS

Startup transients of both torsional and lateral vibration behaviors of an integrally geared centrifugal compressor driven by a synchronous motor are examined by transient torsional-lateral coupled analyses, and the numerical calculation results are evaluated using the field measurement results as a benchmark.

Numerical models of various complexities are employed in the calculations. The numerical simulation confirms that both (a) bilinear stiffness of the pinion rotor bearings due to rotor restraint within the bearing clearance, and (b) detailed torsional-lateral coupled analysis that reflects the effect of temporary teeth separation within the backlash and engagement at the backside because of torque reversal, can strongly affect the calculation results.

The calculated torsional and lateral vibration predictions well match the measurement results. It is shown that the large startup lateral vibration amplitude over 0.4mm(p-p) (16mils(p-p)) can be reasonably replicated by the numerical simulation when bilinear stiffness is considered in the bearing model. Furthermore, the predicted vibration orbits show complex trajectories with abrupt changes in orbital motion similar to those found in the measurements if teeth separation is reflected in the numerical model for the gear meshing.

While these numerical results are satisfactory, in order to further refine the accuracy of the numerical prediction, it is desirable to include either the effects due to the bearing clearance profile of pentagon shape for the bilinear stiffness or the bearing's nonlinear load-displacement relationship that properly accounts for large dynamic displacements of the pinion rotor, i.e. bearing force nonlinearity. Furthermore, transient torque profile during 4.0~4.6sec needs to be more accurately represented. Rotor lifting due to gear mesh engagement upon motor energizing also needs to be accounted for in the numerical simulation.

Despite these limitations, the numerical calculation results reasonably predict the transient lateral vibrational behavior of the pinion rotor, and the overall startup profile is replicated with satisfactory accuracy. Hence, the methodologies described in this paper would be applicable to the design and evaluation of the startup transient phenomena of a synchronous motor driven geared train. With such numerical calculation, more detailed and accurate prediction of the startup events can be feasible for thorough design review. For example, although not shown in this paper, bearing reaction forces during startup can be examined using the numerical simulation result so as to confirm the integrity of the machinery components.

Although the discussion on possible design tuning that may improve the observed high lateral vibration is beyond the scope of this paper, the machinery integrity as per the current design is nevertheless reconfirmed based on this study from several perspectives:
(a) The lateral vibrational amplitudes of the measurement as well as of the calculation stay within the range anticipated in the design
(b) The calculated bearing reaction forces stay within the acceptable magnitude
As such, implementation of the trip bypass with a timer for the pinion rotor's lateral vibration high-high trip function is confirmed to be justifiable.

With the detailed numerical predictions (as the ones done in this paper) during the design phase, adequacy of the protective instrumentation settings to ensure flawless operation of the machinery, such as a trip bypass timer setting, can be more confidently and logically determined so as to certainly cover the entire duration of high lateral vibration occurrence during the motor acceleration. The numerical calculation also enables to confirm the design integrity for the startup transient condition. Through such numerical predictions, it is hoped that the prospects of encountering unpleasant surprises in the field during commissioning of a machinery train may be reduced.

NOMENCLATURE

b	= Backlash	(m) or (in)
$F_{x,b}$	= Lateral force onto bull gear due to gear meshing in horizontal direction	(N) or (lbf)
$F_{x,BL}$	= Contact force due to bilinear stiffness in horizontal direction	(N) or (lbf)
$F_{x,p}$	= Lateral force onto pinion due to gear meshing in horizontal direction	(N) or (lbf)
$F_{y,b}$	= Lateral force onto bull gear due to gear meshing in vertical direction	(N) or (lbf)
$F_{y,BL}$	= Contact force due to bilinear stiffness in vertical direction	(N) or (lbf)
$F_{y,p}$	= Lateral force onto pinion due to gear meshing in vertical direction	(N) or (lbf)
k_{BL}	= Bilinear stiffness	(N/m) or (lbf/in)
k_g	= Mesh stiffness	(N/m) or (lbf/in)
r	= Radial distance between stator center and pinion shaft center $\left(r = \sqrt{{x_p}^2 + \left(y_p - \delta\right)^2}\right)$	(m) or (in)
r_0	= Bearing radial clearance	(m) or (in)
R_b	= Pitch radius of bull gear	(m) or (in)
r_b	= Base radius of bull gear ($r_b = R_b \cos\theta$)	(m) or (in)
R_p	= Pitch radius of pinion	(m) or (in)
r_p	= Base radius of pinion ($r_p = R_p \cos\theta$)	(m) or (in)
T_b	= Torque onto bull gear due to gear meshing	(N-m) or (in-lbf)
T_p	= Torque onto pinion due to gear meshing	(N-m) or (in-lbf)
x_b	= Lateral displacement of bull gear in horizontal direction	(m) or (in)
x_p	= Lateral displacement of pinion in horizontal direction	(m) or (in)
y_b	= Lateral displacement of bull gear in vertical direction	(m) or (in)
y_p	= Lateral displacement of pinion in vertical direction	(m) or (in)
α	= Normal pressure angle	(rad)
β	= Helix angle	(rad)

δ	= Initial offset of pinion shaft center from stator center	(m) or (in)
Δ	= Indicates that the displacement is relative to the location of the latest teeth re-engagement	(-)
θ	= Transverse pressure angle ($\theta = \tan^{-1}(\tan\alpha / \cos\beta)$)	(rad)
φ_b	= Torsional displacement of bull gear	(rad)
φ_p	= Torsional displacement of pinion	(rad)

APPENDIX A (FORMULATION OF GEAR TEETH SEPARATION AND BACKSIDE ENGAGEMENT)

During torque reversal, gear teeth separation and engagement at the backside teeth can occur. When this happens, the meshing forces either disappear or act along the different pressure line, i.e. the pressure line changes depending on whether teeth are engaged in forward direction, separated, or engaged at the backside.

Using the coordinate systems of Figure 33, the relative displacement of the bull gear tooth with respect to the mating pinion tooth along the pressure line can be expressed as in Equation (3).

$$relative\ displacement = \begin{matrix} (x_b - x_p)sin\theta + (y_b - y_p)cos\theta + (r_b\,\varphi_b + r_p\,\varphi_p) & for\ forward\ engagement \\ (x_b - x_p)sin\theta - (y_b - y_p)cos\theta - (r_b\,\varphi_b + r_p\,\varphi_p) & for\ backside\ engagement \end{matrix} \quad (3)$$

Teeth engagement condition can therefore be judged in the following manner, which leads to the teeth engagement criteria of Equation (4) for the torsional-lateral coupled analysis that considers teeth separation and engagement at the backside.

(i) Teeth are engaged in forward direction if $(x_b - x_p)sin\theta + (y_b - y_p)cos\theta + (r_b\,\varphi_b + r_p\,\varphi_p) > 0$
(ii) Teeth are engaged at the backside if $(x_b - x_p)sin\theta - (y_b - y_p)cos\theta - (r_b\,\varphi_b + r_p\,\varphi_p) > b$
(iii) If neither (i) nor (ii) applies, teeth are separated

$$\begin{matrix} (y_b - y_p)cos\theta + (r_b\,\varphi_b + r_p\,\varphi_p) > -(x_b - x_p)sin\theta & \rightarrow & forward\ engagement \\ -(x_b - x_p)sin\theta \geq (y_b - y_p)cos\theta + (r_b\,\varphi_b + r_p\,\varphi_p) \geq -b + (x_b - x_p)sin\theta & \rightarrow & teeth\ separation \\ (y_b - y_p)cos\theta + (r_b\,\varphi_b + r_p\,\varphi_p) < -b + (x_b - x_p)sin\theta & \rightarrow & backside\ engagement \end{matrix} \quad (4)$$

While the teeth are engaged in forward direction, the meshing forces as in Equation (5) are imposed. On the other hand, if the teeth are engaged at the backside, the meshing forces as in Equation (6) are imposed. Furthermore, in case the teeth are separated, no meshing force is imposed. Note that Δ in the below expressions indicates that the displacement relative to the location corresponding to the instant of the latest teeth re-engagement (in either forward or backside direction) after teeth separation needs to be used for the computation.

For forward engagement:

$$\begin{aligned} F_{x,b} &= -k_g sin\theta\left[(sin\theta)\Delta x_b + (cos\theta)\Delta y_b - (sin\theta)\Delta x_p - (cos\theta)\Delta y_p + r_b\,\Delta\varphi_b + r_p\,\Delta\varphi_p\right] \\ F_{y,b} &= -k_g cos\theta\left[(sin\theta)\Delta x_b + (cos\theta)\Delta y_b - (sin\theta)\Delta x_p - (cos\theta)\Delta y_p + r_b\,\Delta\varphi_b + r_p\,\Delta\varphi_p\right] \\ F_{x,p} &= -k_g sin\theta\left[-(sin\theta)\Delta x_b - (cos\theta)\Delta y_b + (sin\theta)\Delta x_p + (cos\theta)\Delta y_p - r_b\,\Delta\varphi_b - r_p\,\Delta\varphi_p\right] \\ F_{y,p} &= -k_g cos\theta\left[-(sin\theta)\Delta x_b - (cos\theta)\Delta y_b + (sin\theta)\Delta x_p + (cos\theta)\Delta y_p - r_b\,\Delta\varphi_b - r_p\,\Delta\varphi_p\right] \\ T_b &= -k_g r_b\left[(sin\theta)\Delta x_b + (cos\theta)\Delta y_b - (sin\theta)\Delta x_p - (cos\theta)\Delta y_p + r_b\,\Delta\varphi_b + r_p\,\Delta\varphi_p\right] \\ T_p &= -k_g r_p\left[(sin\theta)\Delta x_b + (cos\theta)\Delta y_b - (sin\theta)\Delta x_p - (cos\theta)\Delta y_p + r_b\,\Delta\varphi_b + r_p\,\Delta\varphi_p\right] \end{aligned} \quad (5)$$

For backside engagement:

$$\begin{aligned} F_{x,b} &= -k_g sin\theta\left[(sin\theta)\Delta x_b - (cos\theta)\Delta y_b - (sin\theta)\Delta x_p + (cos\theta)\Delta y_p - r_b\,\Delta\varphi_b - r_p\,\Delta\varphi_p\right] \\ F_{y,b} &= -k_g cos\theta\left[-(sin\theta)\Delta x_b + (cos\theta)\Delta y_b + (sin\theta)\Delta x_p - (cos\theta)\Delta y_p + r_b\,\Delta\varphi_b + r_p\,\Delta\varphi_p\right] \\ F_{x,p} &= -k_g sin\theta\left[-(sin\theta)\Delta x_b + (cos\theta)\Delta y_b + (sin\theta)\Delta x_p - (cos\theta)\Delta y_p + r_b\,\Delta\varphi_b + r_p\,\Delta\varphi_p\right] \\ F_{y,p} &= -k_g cos\theta\left[(sin\theta)\Delta x_b - (cos\theta)\Delta y_b - (sin\theta)\Delta x_p + (cos\theta)\Delta y_p - r_b\,\Delta\varphi_b - r_p\,\Delta\varphi_p\right] \\ T_b &= -k_g r_b\left[-(sin\theta)\Delta x_b + (cos\theta)\Delta y_b + (sin\theta)\Delta x_p - (cos\theta)\Delta y_p + r_b\,\Delta\varphi_b + r_p\,\Delta\varphi_p\right] \\ T_p &= -k_g r_p\left[-(sin\theta)\Delta x_b + (cos\theta)\Delta y_b + (sin\theta)\Delta x_p - (cos\theta)\Delta y_p + r_b\,\Delta\varphi_b + r_p\,\Delta\varphi_p\right] \end{aligned} \quad (6)$$

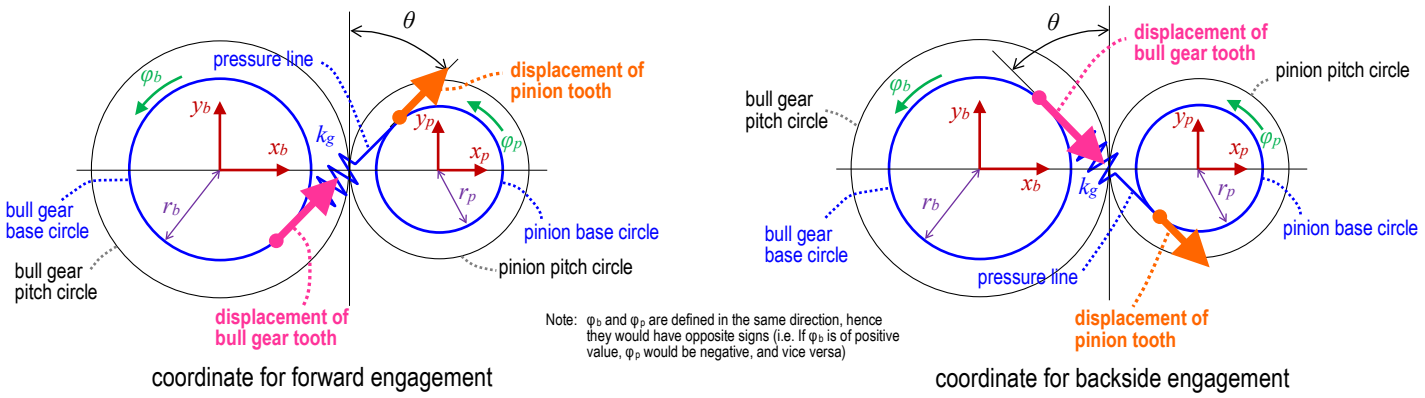

Figure 33. Coordinates for Torsional-Lateral Coupled Analysis with Consideration of Forward and Backside Engagement

REFERENCES

Adachi, A. and Oba, S., 2020, "Overcoming Failure of Synchronous Motor Driven Compressor Train by Application of Controlled Slip Clutch", Proceedings of the Forty-Nineth Turbomachinery Symposium, Texas A&M University.

Adiletta, G., Guido, A. R., and Rossi, C., 1996, "Chaotic Motions of a Rigid Rotor in Short Journal Bearings", Nonlinear Dynamics, *10*, pp.251-269.

API TR684-1, First Edition, 2019, "API Standard Paragraphs Rotordynamic Tutorial: Lateral Critical Speeds, Unbalance Response, Stability, Train Torsionals and Rotor Balancing", American Petroleum Institute.

Cao, J., Allaire, P., and Dimond, T., 2015, "Coupled Lateral and Torsional Nonlinear Transient Rotor-Bearing System Analysis with Applications", Journal of Dynamic Systems, Measurement, and Control, *137*, American Society of Mechanical Engineers.

Cao, J, Dimond, T, and Allaire, P., 2013, "Nonlinear Modeling of Tilting-Pad Bearings with Application to a Flexible Rotor Analysis" Proceedings of the ASME 2013 International Design Engineering Technical Conferences and Computers and Information in Engineering Conference, *8*, American Society of Mechanical Engineers.

Chen, H. M., McLaughlin, D. W. and Malanoski, S. B., 1983, "A Generalized and Simplified Transient Torque Analysis for Synchronous Motor Drive Trains", Proceedings of the Twelfth Turbomachinery Symposium, Texas A&M University.

Chen, W. J., 1995, "Torsional Vibrations of Synchronous Motor Driven Trains Using p-Method", Journal of Vibration and Acoustics, *117*, American Society of Mechanical Engineers.

Corbo, M. A. and Cook, C. P., 2000, "Torsional Vibration Analysis of Synchronous Motor-Driven Turbomachinery", Proceedings of the Twenty-Nineth Turbomachinery Symposium, Texas A&M University.

Corbo, M. A. and Melanoski, S. B., 1996, "Practical Design Against Torsional Vibration", Proceedings of the Twnety-Fifth Turbomachinery Symposium, Texas A&M University.

Ehrich, F. F., 1988, "High-Order Subharmonic Response of High-Speed Rotors in Bearing Clearance", Journal of Vibration, Acoustics, Stress, and Reliability in Design, *110*, pp.9-16.

Friswell, M. I., Penny, J. E., Garvey, S.D. and Lees, A.W., 2010, *Dynamics of Rotating Machines*, Cambridge University Press.

Iannuzzelli, R. J., and Elward, R. M., 1984, "Torsional/Lateral Coupling in Geared Rotors", Turbo Expo: Power for Land, Sea, and Air, *84-GT-71*, American Society of Mechanical Engineers.

Jackson, C. and Leader, M. E., 1983, "Design, Testing and Commissioning of a Synchronous Motor-Gear-Axial Compressor", Proceedings of the Twelfth Turbomachinery Symposium, Texas A&M University.

Maier, M. D. and Studley, G., 2017, "Optimizing Component Selection in Synchronous Motor Compressor Trains Based on Technical and Financial Considerations", Proceedings of the Forty-Sixth Turbomachinery Symposium, Texas A&M University.

Mruk, G. K., 1978, “Compressor Response to Synchronous Motor Startup”, Proceedings of the Seventh Turbomachinery Symposium, Texas A&M University.

Oscarson, G., Imbertson, J., Imbertson, B., and Moll, S., 1954, “The ABC’s of Synchronous Motors”, Electric Machinery Company.

Pradetto, J. C. and Baumann, U., 2015, “Coupled Torsional and Lateral Analysis for the Determination of the Damping of the First Torsional Mode of Synchronous Motor Driven Compressor Trains”, Forty-Fourth Turbomachinery Symposium, Texas A&M University.

Rao, J. S., Shiau, T. N., and Chang, J. R., 1998, “Theoretical Analysis of Lateral Response Due to Torsional Excitation of Geared Rotors”, Mechanism and Machine Theory, *33*, pp.761-783.

Sciancalepore, M., Beretta, A., and Satish, H., 2019, “Torsional Rotordynamic Excitation, Natural Frequency and Damping Characteristics in a Viscous Centrifugal Pump Application”, Proceedings of the Thirty-Fifth International Pump Users Symposium, Texas A&M University.

Szenasi, F. R. and von Nimitz, W. W., 1978, “Transient Analyses of Synchronous Motor Trains”, Proceedings of the Seventh Turbomachinery Symposium, Texas A&M University.

Yeiser, C. W., Hutten, V., Ayoub, A. and Rheinboldt, R., 2006, “Revamping a Gas Compressor Drive Train from 7000 to 8000 HP with a New Synchronous Motor Driver and a Controlled Slip Clutch Mechanism”, Proceedings of the Thirty-Fifth Turbomachinery Symposium, Texas A&M University.

Wachel, J. C. and Szenasi, F. R., 1993, “Analysis of Torsional Vibrations in Rotating Machinery”, Proceedings of the Twenty-Second Turbomachinery Symposium, Texas A&M University.

Wang, Q., Feese, T. D. and Pettinato, B. C., 2012, “Torsional Natural Frequencies: Measurement vs. Prediction”, *Proceedings of the Forty-First Turbomachinery Symposium*, Texas A&M University.